J Solid State Electrochem (2014) 18:2555–2562
DOI 10.1007/s10008-014-2512-1

ORIGINAL PAPER

Insights into electrocatalytic activity of epitaxial graphene on SiC from cyclic voltammetry and ac impedance spectroscopy

Paweł Szroeder · Nikos G. Tsierkezos · Mariusz Walczyk · Włodzimierz Strupiński · Agnieszka Górska-Pukownik · Janusz Strzelecki · Kamil Wiwatowski · Peter Scharff · Uwe Ritter

Received: 12 September 2013 / Revised: 5 May 2014 / Accepted: 7 May 2014 / Published online: 24 May 2014

Abstract Electrocatalytic activity of graphene grown epitaxially on SiC is studied using cyclic voltammetry and electrochemical impedance spectroscopy. AFM images show step-like topography of SiC-graphene. For ferri-/ferrocyanide redox couple, no voltammetric response is observed at the pristine graphene. Basal planes of graphite are electrochemically inactive as well. After electrochemical oxidation, apparent redox peaks appear at both the graphene and graphite electrode. However, more intensive redox peaks are observed at graphene, where simultaneous redox reaction with the adsorbed and the diffused ferri-/ferrocyanide ions occurs. Electrochemical impedance measurements show that the graphene electrode behaves like an array of microelectrodes. We used the partially blocked electrode model to fit impedance data. Using the fitting parameters, a size of microelectrodes was found to be 23.8±2.1 μm and the active surface of graphene was estimated to be 21 %. A value of the standard electron transfer rate constant found for the anodized epitaxial graphene $(2.16\pm0.32)\times10^{-3}\mathrm{cm}\cdot\mathrm{s}^{-1}$) is by one order of magnitude lower than the standard rate constant estimated for the anodized graphite basal planes ($\sim5\times10^{-2}\mathrm{cm}\cdot\mathrm{s}^{-1}$). Electrochemical reduction causes total disappearance of electrochemical responses at the graphene electrode, whereas only slight decrease of the peak currents is observed at the reduced graphene. Such behavior proves that different activation mechanisms occur at the graphene and graphite electrodes.

Keywords Epitaxial graphene · Cyclic voltammetry · Electrochemical impedance spectroscopy · Standard electron transfer rate constant

Introduction

The successful development of graphene-based electrochemical sensors and energy storage systems depends on large-scale availability of the material. Single- and few-layer graphene was successfully isolated for the first time by Boehm in 1962 [1]. But global efforts to investigate and exploit graphene properties have got underway since Novoselov et al. [2] discovered a simple method of graphene manufacturing by mechanical exfoliation of bulk graphite.

The widely used large-scale method of graphene fabrication is the reduction of graphene oxide [3, 4]. Glassy carbon electrodes modified with reduced graphene oxide demonstrate fast electron transfer [5] and possess good effectiveness toward simultaneous detection of ascorbic acid, dopamine, and serotonin [6, 7]. The DNA-bases sensors on the base of reduced graphene oxide were prepared as well [8].

Continuous graphene layers are grown successfully by chemical vapor deposition of hydrocarbons onto transition metal substrates [9–12]. As revealed by electrochemical cell microscopy experiments, the heterogeneous electron transfer

Electronic supplementary material The online version of this article (doi:10.1007/s10008-014-2512-1) contains supplementary material, which is available to authorized users.

P. Szroeder (✉) · A. Górska-Pukownik · J. Strzelecki · K. Wiwatowski
Instytut Fizyki, Wydział Fizyki, Astronomii i Informatyki Stosowanej, Uniwersytet Mikołaja Kopernika, Grudziądzka 5, 87-100 Toruń, Poland
e-mail: psz@fizyka.umk.pl

N. G. Tsierkezos · P. Scharff · U. Ritter
Institut für Chemie und Biotechnik, Technische Universität Ilmenau, Weimarer Str. 25, 98693 Ilmenau, Germany

M. Walczyk
Wydział Chemii, Uniwersytet Mikołaja Kopernika, ul. Gagarina 7, 87-100 Toruń, Poland

W. Strupiński
Instytut Technologii Materiałów Elektronicznych, Wólczyńska 133, 01-908 Warszawa, Poland

rate increases with the number of graphene layers [13]. Another important factor determining the electrocatalytic activity of this material is the graphene layer stacking. A considerable disadvantage of CVD-grown graphene is that transfer to a semi-insulating or insulating substrate is required before using them as electrodes.

That is one of the reasons for developing a method of single- or few-layer graphene preparation by thermal decomposition of SiC [14, 15]. In this method, epitaxial graphene (EG) is grown directly on the semi-insulating SiC substrate. However, because decomposition of SiC is not a self-limiting process, regions with different number of graphene layers coexist [16, 17], giving rise to non-homogeneous electrocatalytic activity of the EG electrode.

The present work derives from our conviction that there is a correlation between efficiency of redox reactions occurring at the EG electrode and structure of interfacial water at graphene buffer layer, G_0, and subsequent G_n layers of intrinsic graphene. The interaction of the interfacial water with EG grown on SiC has been studied theoretically [18, 19] and experimentally by frequency modulation AFM [20], high-resolution X-ray analyses [21], vibrational spectroscopy [22], and contact angle goniometry [23]. It has been shown that the G_0 containing high number of sp^3 carbon-bonded inclusions chemically bonds the closest lying water molecules and, probably, blocks electrochemical reactions at the interface.

To verify the conjecture of the blocking character of G_0, we have carried out cyclic voltammetry (CV) and electrochemical impedance spectroscopy (EIS) experiments at EG electrode. CV data obtained at EG electrode were compared with graphite. We have chosen $Fe(CN)_6^{3-/4-}$ as a benchmark system. This redox pair is very sensitive to the state of the surface and has been used in the investigations of electrocatalytic activity of carbon electrodes [24].

EG was characterized using Raman spectroscopy and AFM. Due to rather poor electrocatalytic activity of intrinsic graphene and graphite [25–27], the electrodes were activated by anodization [28, 29]. It has been shown that during electrochemical oxidation, several functional groups connect to the graphite basal plane and many multivacancies and small etch pits appear [30]. As it was noticed in [31], the activation of graphite toward $Fe(CN)_6^{3-/4-}$ redox reaction is rather related to the lattice damage than surface oxides. As we show, redox reactions of $Fe(CN)_6^{3-/4-}$ occur at both the anodized graphite and EG. To resolve the question whether surface functional groups, which are unresistant to the reduction, or more stable topological defects are responsible for catalytic activity of electrodes, the CV tests were repeated at electrochemically reduced electrodes. Results suggest different activation mechanism at graphite basal planes and EG.

Models assuming both the uniform diffusion at homogeneous flat electrode and the radial diffusion at partially blocked flat electrode (PBE) were considered in the discussion of the ac electrochemical impedance data. Experiments and simulations provide new insights into processes occurring at the EG electrode. Particularly, it has been shown that only 21 % of the surface of EG is electrocatalytically active. Our observations bear important implications for the understanding and control of the electrocatalytic activity of the EG.

Experimental setup

EG was fabricated on the silicon face of highly purity SiC-H. Details for the growth of epitaxial graphene have been published [15]. Commercial highly oriented pyrolytic graphite (HOPG) plate of grade ZYH (Materials Quartz Inc.®) was also used as a bulk graphite electrode. Samples were characterized by Raman spectroscopy and AFM. Raman spectra were measured using inVia spectrometer (Renishaw, Gloucestershire, UK) at laser excitation light of the length of 488 nm in a backscattering geometry. Surface morphology was imaged in contact mode using an Agilent 5500 AFM/SPM microscope.

The anodization was carried out by applying a potential of + 1.5 V vs. Ag/AgCl for 1,000 s in pH 7 phosphate buffer solution. Much better wetting of the oxidized electrodes was observed with the naked eye. After electrochemical measurements, the electrodes were reduced in the same buffer solution at potential of −1.2 V vs. Ag/AgCl for 1,000 s. Chronoamperometric curves recorded during anodization and reduction process are presented in Fig. S1 of Supplementary Material.

CVs were recorded using a computer-controlled Autolab (Eco Chemie) modular electrochemical system equipped with a PGSTAT128N potentiostat, controlled by NOVA software. The measurements were carried out using a three-electrode electrochemical cell. The effect of the uncompensated resistance was reduced by applying the positive feedback technique. HOPG plate 1.0×1.0×0.1 cm in size and the EG grown on SiO_2/SiC 1.0×1.0 cm in size were used as the working electrodes. Details concerning geometry of contacts are described in Supplementary Material. The counter electrode was a Pt wire, and the reference electrode was Ag/AgCl (3 mol·L^{-1} KCl). CVs were recorded for 1 mmol·L^{-1} $K_4Fe(CN)_6$ with scan rates, υ, ranging from 20 to 200 mV·s^{-1}. As a supporting electrolyte, an aqueous solution of 1 mol·L^{-1} KCl was used. All measurements were carried out in the thermostated system at the room temperature (293 K).

The EIS spectra were measured using computer-controlled system Zahner/IM6/6EX. We have done the experiments in the potentiostatic mode, at a fixed DC potential equal to the half-wave potentials derived from the CV spectra. A sinusoidal signal of very small amplitude of 10 mV in the frequency range from 1 Hz to 1 MHz was superimposed on the DC

potential. The resulting current was measured to determine the impedance.

Measurements were performed at the graphene working electrode against the reference electrode Ag/AgCl (3 mol·L^{-1} KCl), while the Pt plate (area of 2 cm^2) served as a counter electrode. Both the CV and EIS measurements were carried out at the standard ambient temperature of 293 K. The EIS data were analyzed using EIS Spectrum Analyser Freeware [32]. Fitting to the partially blocked electrode model was done using Matlab® procedures for solving the non-linear least squares problems.

Results and discussion

In the AFM image shown in Fig. 1a, b, a characteristic step-like topography of SiC substrate is seen. The steps are 1–2-μm wide and about 1.2-nm tall. The graphene layers grow on the SiC step edges, where excess of C atoms diffusing across the substrate is produced [16, 17]. Layers G_1 and G_2 of the intrinsic graphene and the SiC substrate are separated by the graphene buffer layer G_0, which contains high number of sp^3 carbon-bonded inclusions. The EG surface is inhomogeneous; there are steps where one or two layers of graphene have grown and steps covered only with G_0.

Raman spectra of HOPG and EG are dominated by G band and their second-order counterpart G′ which are typical for sp^2 carbon-bonded systems [33, 34]. In EG, an additional D mode appears, which is active in disordered systems. Using the procedure proposed by Lucchese [35, 36], on the base of the intensity ratio of D and G band, I_D/I_G=1.6, an averaged distance between defects was estimated ~7 nm. Large intensities of I_D prove high contribution of area covered with highly disordered G_0 in the EG surface.

CVs obtained at the EG and HOPG electrodes are shown in Fig. 2. No electrochemical response for $Fe(CN)_6^{3-/4-}$ is observed at pristine electrodes. These results coincide with the observed low electrocatalytic activity of the EG toward oxygen reduction reaction [37]. After anodization, apparent peaks appear with half-wave potentials of $E_{1/2}$=0.268V vs. Ag/AgCl and $E_{1/2}$=−0.025V vs. Ag/AgCl for HOPG and EG, respectively. We have estimated the $E_{1/2}$ for EG from the CV obtained at the lowest scan rate, at which quasi-reversible reaction occurs. Because of asymmetry of CV curves at the EG, estimated value of the formal potential is approximate. Oxidation and reduction peaks disappear at the EG electrode

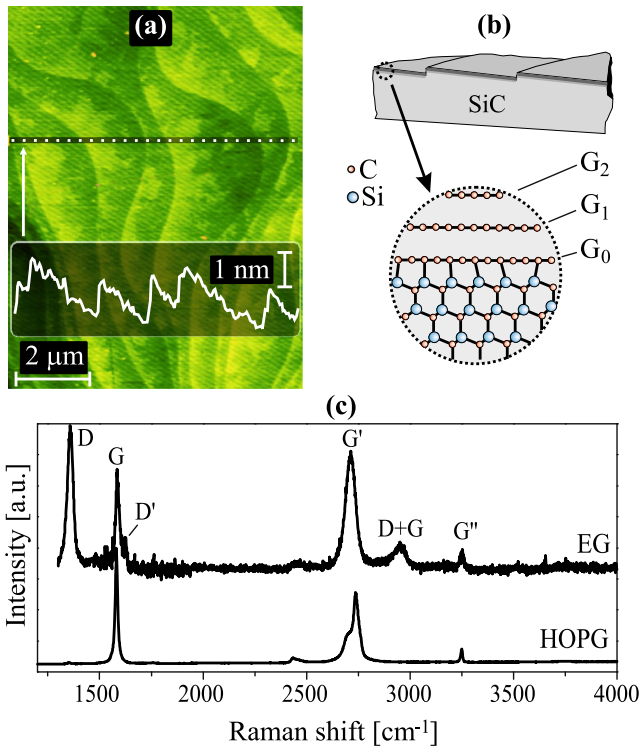

Fig. 1 (Color online) **a** AFM image of graphene grown on SiC substrate. *Inset*: profile across a dotted line shows steps in the underlying SiC substrate (about 1.2-nm tall). **b** Schematic of the SiC substrate with the epitaxially grown graphene. Below, a structural model with buffer graphene layer, G_0, and subsequent layers, G_1 and G_2, is shown. **c** Raman spectra of HOPG and EG

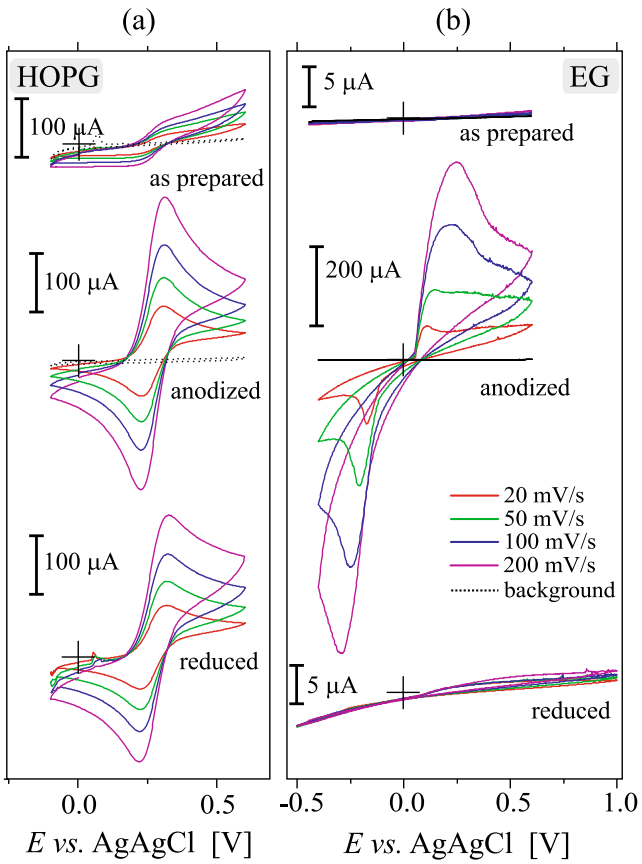

Fig. 2 (Color online) CV plots recorded for $Fe(CN)_6^{3-/4-}$ redox couple in KCl supporting electrolyte at pristine, anodized, and cathodically treated HOPG (**a**) and EG (**b**)

after electrochemical reduction in buffer solution. As it is seen in Fig. 2a, the same treatment causes only slight decrease of the oxidation and reduction peak currents at the HOPG electrode.

A dependence of the oxidation peak current, i_p^{Ox}, on the square root of the scan rate, $v^{1/2}$, at the HOPG and EG electrode is presented in Fig. 3. Anodic peak current at the HOPG electrode increases linearly with $v^{1/2}$ indicating a chemically reversible redox process. Using the Randles–Ševčik equation,

$$i_p^{Ox} = 2.685 \cdot 10^5 z^{3/2} A v^{1/2} D^{1/2} c, \quad (1)$$

where z is a number of transfered electrons exchanged in the redox reaction, A is the active surface of the electrode in square centimeters, D is the diffusion coefficient [$cm^2 \cdot s^{-1}$], and c is the concentration of oxidized species [$mol \cdot cm^{-3}$]; the diffusion coefficient was calculated. Its value estimated from the slope coefficient, B, was found to be $(7.1 \pm 0.8) \times 10^{-6} cm^2 \cdot s^{-1}$. To the uncertainty of the result mainly contributes low accuracy of the active area of the HOPG ($0.85 \pm 0.05 cm^2$). Even so, similar values for $Fe(CN)_6^{3-/4-}$ redox couple in aqueous KCl solution were reported in [38, 39].

CV curves recorded at the EG electrode are asymmetric ($i_p^{Ox}/i_p^{Red}=0.75$), which indicates the irreversible redox reaction. In the investigated scan rates range, separation of the anodic and cathodic peak potentials also shows quasi-reversible and irreversible responses, suggesting a blocked surface (see Figure S4 in Supplementary Material).

On the other hand, the anodic current peaks are much more intensive than peaks observed at the HOPG electrode. As it is shown in Fig. 3, the peak current dependence on $v^{1/2}$ for EG can be fitted to the quadratic function, $y=Cx+Dx^2$, where $x=v^{1/2}$ and $y=i_p^{Ox}$. Non-zero value of the fitting parameter D suggests that the peak current is not limited by diffusion of $Fe(CN)_6^{3-/4-}$. That means that the observed peak current is partially due to a reaction of the redox couple adsorbed at the electrode and partially due to a reaction of $Fe(CN)_6^{3-/4-}$ diffusing through the diffusion layer. It is important to note that the reduction process of the adsorbed redox species is more efficient than oxidation. This probably indicates higher adsorption ability of $Fe(CN)_6^{3-}$ than $Fe(CN)_6^{4-}$. The different adsorption ability of $Fe(CN)_6^{3-}$ and $Fe(CN)_6^{4-}$ causes the negative shift of redox potential at the EG electrode as compared to HOPG.

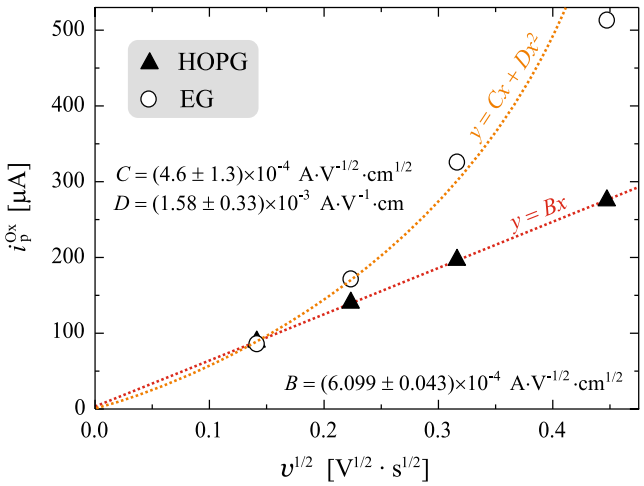

Fig. 3 (Color online) The dependence of the anodic peak current on the square root of the scan rate for HOPG and EG fitted to the linear and quadratic function

As it is seen, the deviation from the quadratic dependence is observed at higher scan rates. This deviation can be attributed to high resistance of the electrode and to the lateral diffusion at microelectrodes, which causes decrease of the peak currents with increasing scan rate [40, 41].

Opposite to the HOPG, the EG electrode loses its electrocatalytic properties after electrochemical reduction. This finding as well as higher peak currents at the EG showed different activation mechanisms at basal graphite plane and epitaxially grown graphene. Probably, redox mediation by functional groups (e. g., quinones) occurs at the EG electrode, whereas edge planes and other zero and one-dimensional surface defects are responsible for catalytic activity of HOPG toward $Fe(CN)_6^{3-/4-}$. As the surface functional groups are not resistant to the electrochemical reduction, the electrochemical response disappear at the reduced EG electrode. On the other hand, surface defects do not disappear after reduction of HOPG.

The uniform diffusion-controlled mass transport phenomena through the solid–liquid interface are well described within the Nicholson theory [42]. Using the procedure described in [43] and Figure S4 of Supplementary Material, the standard heterogeneous electron transfer rate constant, k_s, of the electron transfer between $Fe(CN)_6^{3-/4-}$ and the anodized HOPG was roughly estimated to $\sim 5 \times 10^{-2} cm \cdot s^{-1}$. As the separation of peak potentials are large at the EG electrode (Figure S4 of Supplementary Material), the use of the Nicholson procedure would be irrelevant. Theoretical value of the standard rate constant for interfacial charge transfer between a semi-metallic electrode and $Fe(CN)_6^{3-/4-}$ was calculated to 2.8×10^{-4} $cm \cdot s^{-1}$ [44]. For basal planes of the pristine HOPG, the observed value of k_s is less than 10^{-6} $cm \cdot s^{-1}$ [45]. Low electron transfer kinetics at semi-metallic electrodes is a consequence of the low density of states at the Fermi level [46]. Electrochemical oxidation leads to the disruption of the surface basal planes and destruction of their semi-metallic character, that permits increase of electron transfer rate by a 10^4 factor. Theoretical calculations show that defects introduced into graphene planes induce additional electron states near the Fermi level [47]. As it is demonstrated in [36], disorder-induced states contribute to electrochemical performance of carbon nanotube and graphene electrodes.

As the presented above CV data deliver no clinching arguments for the question, if the EG can be considered as an array of partially blocked electrodes, the EIS experiments were performed at this electrode. EIS data in the Nyquist and Bode representation are shown, respectively, in Fig. 4a, b. In addition, Bode diagrams for real and imagined part of impedance are plotted in Figure S6 of Supplementary Materials.

Nyquist plot consists of two semicircles in high- and intermediate-frequency region, which are followed by an irregular line in low-frequency region. The semicircle at high frequencies corresponds to silver/graphene interface, which is represented by contact resistance, R_{int}, and interface capacitance, C_{int}. The large semicircle in the intermediate-frequency region arises due to the electron transfer through electrolyte/graphene interface. Bode plot shows phase angle dependence as a function of frequency. The maximum at 1.6 kHz refers to the top of the semicircle in the intermediate-frequency region of Nyquist plot. Below 135 Hz, the dependence of phase angle on frequency is rather weak. It corresponds to the *quasi*-linear part of the Nyquist plot and represents the diffusionally limited electrochemical process.

In Fig. 4c, extended Randles–Erschler equivalent circuit is shown, which consists of double-layer capacitance, C_{dl}, connected in parallel with charge transfer resistance, R_{ct}, in series with the Warburg/PBE impedance, $Z_{W,PBE}$. The intercept of the Nyquist plot with real axis of impedance in high-frequency region corresponds to the resistance of electrolyte represented by R_e [48]. An additional RC circuit in parallel consisting of silver/graphene interface resistance, R_{int}, and silver/graphene interface capacitance, C_{int}, was connected in series to the Randles–Erschler equivalent circuit. The equivalent circuit parameters fitted to experimental data using the Warburg (uniform diffusion) and PBE impedance (non-uniform diffusion) are compared in Table 1.

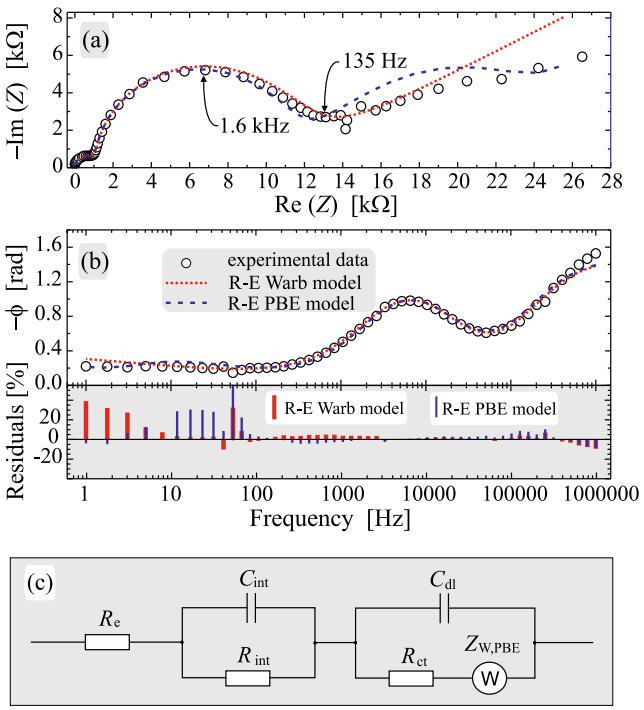

Fig. 4 (Color online) **a** Nyquist and **b** Bode plots of the EIS data obtained at the EG electrode. **c** Extended Randles–Erschler equivalent circuit used for evaluation of the electrode, interface, and electrolyte parameters. EIS data were modeled with Warburg impedance (R–E Warb) and PBE impedance (R–E PBE). At the bottom of Bode plot, residuals from the fitted models are shown

It should be noted that at frequencies higher than 100 kHz, beyond the electrolyte, electrode, and contact resistance/capacitance, the inductance of the electrochemical cell and external wires affects the impedance. The inductance can interfere with pure resistance/capacitance of the contact, resistance of electrode, and resistance of the solution. Due to this interferences, the value of R_e was estimated with relative standard error higher than 50 %. To determine the value of the solution resistance, we have carried out the series of EIS experiments at metallic and glassy carbon electrodes (Figure S7 of the Supplementary Material). Results show that the serial resistance at metallic and glassy carbon electrode is no higher than 40 Ω.

The tail at low frequencies pertains to the diffusion of ions into the bulk of electrolyte. It is represented by the Warburg impedance, $Z_W=\sigma^*/(j\omega)^n$, where $j=\sqrt{-1}$ and ω is the angular frequency. When uniform diffusion occurs in semi-infinite space, the slope of linear part of the Nyquist plot is equal to 1, the phase angle in the Bode plot is equal to 0, and n=0.5. For this ideal Warburg impedance, the σ^* parameter has a meaning of Warburg coefficient, σ, given by the formula

$$\sigma = \frac{\sqrt{2}RT}{z^2F^2Ac\sqrt{D}}. \quad (2)$$

Table 1 Fitting parameters and their standard errors for EIS data obtained at the EG electrode using equivalent circuit from Fig. 5c

Model	R–E Warb	R–E PBE
C_{int}[×10^{-10}F]	8.91±0.53	9.6±1.4
R_{int}[kΩ]	1.042±0.037	1.041±0.096
C_{dl}[×10^{-9}F]	7.69±0.49	7.67±0.12
R_{ct}[kΩ]	9.22±0.28	9.98±0.10
σ^*[×10^{4}Ω·s^{-n}]	3.05±0.23	1.125±0.068
n	0.308±0.014	0.5
θ	–	0.785±0.016
q[rad·s^{-1}]	–	32.3±1.8
R_e [Ω]	7.1±4.8	7.2±5.6
σ_{res}[Ω]	569.14	543.89

Column "R–E Warb" corresponds to the model containing the Warburg impedance Z_W, whereas column "R–E PBE" corresponds to the circuit with PBE impedance, Z_{PBE}. Parameter σ_{res} is the standard deviation of residuals

Here, R is the universal gas constant (8.314 $J \cdot mol^{-1} \cdot K^{-1}$), and T is the absolute temperature, $F=9.6484\times10^4$ $C \cdot mol^{-1}$ is the Faraday constant. However, the slope of experimental data in the Nyquist plot at low frequency is less than 1, and the phase angle in Bode plot is non-zero as well. The fitting procedure performed using Warburg impedance in Randles–Erschler circuit gives value of $n=0.308\pm0.014$, suggesting rather non-uniform diffusion at the EG electrode. Note, that no CPE were used in the approximations.

From the literature, it is known that SiC substrate influences significantly the interaction of interfacial water with EG [20, 21, 49]. Particularly, this concerns the areas covered only with buffer layer G_0 [21]. The Raman and AFM data presented above suggest that EG should be rather considered as an array of intrinsic graphene domains, G_n, which are embedded in G_0-SiC plane. Thus, EG should be treated as PBE with non-active and active domains, which are depicted in Fig. 5. According to PBE model [40, 41, 50–52], the diffusion impedance is determined by the Warburg coefficient σ and coverage of the blocking layer, θ. The active area of microelectrode is represented as $1-\theta$. When microelectrodes are disk-shaped, then

$$1-\theta = \frac{r_a^2}{r_0^2}. \tag{3}$$

Here, r_a is the radius of the active part of the microelectrode and r_0 is the radius of the whole domain surrounding the active part.

When the whole area of the electrode is active, i.e., $r_a=r_0$, the coverage of blocking layer $\theta=0$ and the total diffusion impedance of the electrode is equal to infinite Warburg impedance, Z_W. For $0<\theta<1$, diffusion impedance of PBE is given by the formula [41, 52]

$$Z_{PBE} = \frac{\sigma}{\sqrt{\omega}}\left[1+\frac{\theta}{1-\theta}\left(\frac{(1+q^2/\omega^2)+q/\omega}{1+(q/\omega)^2}\right)^{1/2} + j + \frac{j\theta}{1-\theta}\left(\frac{(1+q^2/\omega^2)-q/\omega}{1+(q/\omega)^2}\right)^{1/2}\right], \tag{4}$$

where q is the characteristic frequency of lateral diffusion within non-homogeneous diffusion layer (see Fig. 5). For $1-\theta>0.1$, the expression of q parameter is [41, 52]

$$q = \frac{2D}{r_0^2\theta(1-\theta)ln\left(1+0.27/\sqrt{1-\theta}\right)}. \tag{5}$$

According to the fitting results collected in Table 1 and residuals of phase angle presented in Fig. 4b, the PBE model is more suitable to the investigated system at frequencies lower than 10 Hz. Standard deviation of residuals, σ_{res}, are comparable for both models, but the σ^* parameter in the term Z_W, which is responsible for the diffusion has no clear physical meaning for $n\neq0.5$. Furthermore, the behavior of the real system is reflected quite good in the PBE model at low frequencies, when overlapping of the diffusion profiles of microelectrodes occurs.

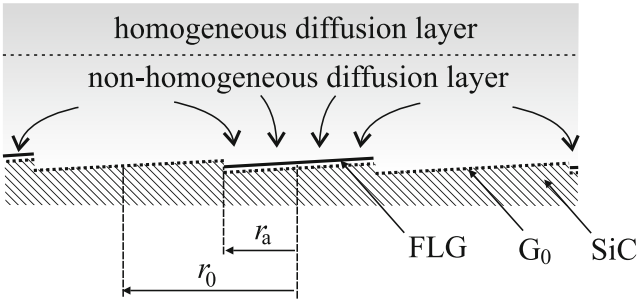

Fig. 5 EG as a partially blocked electrode. Areas of the G_0-SiC covered with intrinsic graphene layers, G_n, are electrocatalytically active. Directly above the interface, the lateral non-homogeneous diffusion represented by impedance Z_{BPE} occurs

Using expressions 3 and 5, data from the Table 1, and diffusion coefficient determined from CV experiments, the radius of the microdomain in EG, r_0, and radius of the electroactive part of microelectrode, r_a, were estimated to, respectively, 23.8±2.1 and 11.1±1.3μm. Note that obtained results concern the disk-shaped microelectrode array model, while the EG electrode forms an array of stripes of width of 1−2μm and length of tens or hundreds of micrometers (see Fig. 1a). The estimated value of Warburg coefficient, $\sigma=(1.125\pm0.068)\times10^4\Omega \cdot s^{-1/2}$, was used for calculation of the active surface of the EG electrode. Using Eq. 2, the active surface was found to be $A=(1.23\pm0.15)\times10^{-2}cm^2$.

Charge transfer resistance depends on the exchange current i_0 at equilibrium, according to

$$R_{ct} = \frac{RT}{zFi_0}, \tag{6}$$

where $i_0=zFAk_sc$. Using Eq. 6, a value of the standard electron transfer rate constant between EG and $Fe(CN)_6^{3-/4-}$ was calculated to $(2.16\pm0.32)\times10^{-3}cm \cdot s^{-1}$.

It should be noted that reduction of $Fe(CN)_6^{3-}$ at graphene has been extensively studied by Valota et al. [39]. Electron transfer rate constant for exfoliated graphene with very low defect density on Si/SiO_2 was found to be 1.2×10^{-3} $cm \cdot s^{-1}$. According to the results presented by us, the pristine HOPG basal planes and the pristine EG are electrochemically inactive, what contradicts to the findings of Valota. Probably, besides of defects and surface functional groups, substrate is an important factor, which enhances or hinders electrocatalytic activity of graphene electrodes. Influence of substrate and surface morphology of the EG (number of intrinsic layers,

defect density) on its electrocatalytic activity is the focus of ongoing work.

Conclusions

At both the pristine EG and HOPG basal plane electrodes, redox reaction does not occur. Electrochemical oxidation causes a change of electrocatalytic activity. However, evident difference in the behavior of the EG and graphite is observed. While at the oxidized basal planes of HOPG redox reactions are reversible, the EG behaves as a partially blocked electrode. The CV and EIS data suggesting that the EG is an array of microelectrodes are supported by AFM images, in which not homogeneous, step-like surface topography is clearly seen. Furthermore, the intensive D-line in the Raman spectrum is an indicative of high content of defects, which are characteristic to the buffer graphene layer G_0.

The EG shows transient activity toward $Fe(CN)_6^{3-/4-}$ and high redox peak currents after activation, as compared with HOPG. This behavior suggest that there are two different activation mechanisms of redox reaction in EG and HOPG. In the first case, unstable surface functional groups are responsible for both the adsorption of $Fe(CN)_6^{3-/4-}$ and redox mediation. Functional groups disappear after electrochemical reduction and the EG loses its electrocatalytic properties. In the second case, electrocatalytic activity of basal planes of graphite is responsible for more stable lattice defects, which are resistant against reduction. Therefore, the HOPG electrode is active after electrochemical treatment with cathodic current.

Acknowledgments Authors would like to thank Mrs. D. Schneider (TU Ilmenau) for performing EIS experiments.

References

1. Boehm HP, Clauss A, Fischer GO, Hofmann U (1962) Z Naturforsch B 17:150–153
2. Novoselov KS, Geim AK, Morozov SV, Jiang D, Zhang Y, Dubonos SV, Grigorieva IV, Firsov AA (2004) Science 306:306–309
3. Gilje S, Han S, Wang M, Wang KL, Kaner RB (2007) Nano Lett 7: 3394–3398
4. Stankovich S, Dikin DA, Piner RD, Kohlhaas KA, Kleinhammes A, Jia Y, Wu Y, Nguyen ST, Ruoff RS (2007) Carbon 45:1558–1565
5. Tang L, Wang Y, Li Y, Feng H, Lu J, Li J (2009) Adv Funct Mater 19: 2782–2789
6. Alwarappan S, Erdem A, Liu C, Li C-Z (2009) J Phys Chem C 113: 8853–8857
7. Kim Y-R, Bong S, Kang Y-J, Yang Y, Mahajan RK, Kim JS, Kim H (2010) Biosens Bioelectron 25:2366–2369
8. Zhou M, Zhai Y, Dong S (2009) Anal Chem 81:5603–5613
9. Kim KS, Zhao Y, Jang H, Lee SY, Kim JM, Kim KS, Ahn J-H, Kim P, Choi J-Y, Hong BH (2009) Nature 457:706–709
10. Li X, Cai W, An J, Kim S, Nah J, Yang D, Piner R, Velamakanni A, Jung I, Tutuc E, Banerjee SK, Colombo L, Ruoff RS (2009) Science 324:1312–1314
11. Srivastava A, Galande C, Ci L, Song L, Rai C, Jariwala D, Kelly KF, Ajayan PM (2010) Chem Mater 22:3457–3461
12. Mattevi C, Kim H, Chhowalla M (2011) J Mater Chem 21:3324–3334
13. Güell AG, Ebejer N, Snowden ME, Macpherson JV, Unwin PR (2012) J Am Chem Soc 134:7258–7261
14. Emtsev KV, Bostwick A, Horn K, Jobst J, Kellogg GL, Ley L, McChesney JL, Ohta T, Reshanov SA, Rohrl J, Rotenberg E, Schmid AK, Waldmann D, Bweber H, Seyller T (2009) Nat Mater 8:203–207
15. Strupinski W, Grodecki K, Wysmolek A, Stepniewski R, Szkopek T, Gaskell PE, Gruneis A, Haberer D, Bozek R, Krupka J, Baranowski JM (2009) Nano Lett 11:1786–1791
16. Biedermann LB, Bolen ML, Capano MA, Zemlyanov D, Reifenberger RG (2009) Phys Rev B 79:125411(10)
17. Ohta T, Bartelt NC, Nie S, Thürmer K, Kellogg GL (2010) Phys Rev B 81:121411
18. Gordillo MC, Martí J (2008) Phys Rev B 78:075432
19. Ma J, Michaelides A, Alfe D, Schimka L, Kresse G, Wang E (2011) Phys Rev B 84:033402
20. Suzuki K, Oyabu N, Kobayashi K, Matsushige K, Yamada H (2011) Appl Phys Express 4:125102
21. Zhou H, Ganesh P, Presser V, Wander MCF, Fenter P, Kent PRC, Jiang D, Chialvo AA, McDonough J, Shuford KL, Gogotsi Y (2012) Phys Rev B 85:035406
22. Politano A, Marino AR, Formoso V, Chiarello G (2011) Carbon 49: 5180–5184
23. Shin YJ, Wang Y, Huang H, Kalon G, Wee ATS, Shen Z, Bhatia CS, Yang H (2010) Langmuir 26:3798–3802
24. McCreery RL (2008) Chem Rev 108:2646–2687
25. Brownson DAC, Banks CE (2010) Analyst 135:2768–2778
26. Brownson DAC, Banks CE (2011) Phys Chem Chem Phys 13: 15825–15828
27. Brownson AC, Foster CW, Banks CE (2012) Analyst 137: 1815–1823
28. Lim CX, Hoh HY, Ang PK, Loh KP (2010) Anal Chem 82: 7387–7393
29. Dubuisson E, Yang Z, Loh KP (2011) Anal Chem 83:2452–2460
30. Nose M, Kinumoto T, Choo H-S, Miyazaki K, Abe T, Ogumi Z (2009) Fuel Cells 3:284–290
31. McDermott CA, Kneten KR, McCreery RL (1993) J Electrochem Soc 140:2593–2599
32. Bondarenko AS, Rogoisha GA (2014) EIS spectrum analyser http://www.abc.chemistry.bsu.by/vi/analyser/ Accessed 12 Mar 2014
33. Basko D, Piscanec S, Ferrari A (2009) Phys Rev B 80:165413
34. Casiraghi C, Pisana S, Novoselov K, Geim A, Ferrari A (2007) Appl Phys Lett 91:233108
35. Lucchese M, Stavale F, Martins Ferreira E, Vilani C, Moutinho M, Capaz R, Achete C, Jorio A (2010) Carbon 48:1592–1597
36. Szroeder P, Górska A, Tsierkezos NG, Ritter U, Strupiński W (2013) Materialwiss Werkst 44:226–230
37. Szroeder P, Tsierkezos NG, Ritter U, Strupiński W (2013) J Nanosci Lett 3:9
38. Konopka SJ, McDuffie B (1970) Anal Chem 42:1741–1746
39. Valota AT, Kinloch IA, Novoselov KS, Casiraghi C, Eckmann A, Hill E, Dryfe RAW (2011) ACS Nano 5:8809–8815
40. Gueshi T, Tokuda K, Matsuda H (1979) J Electroanal Chem 101:29–38

41. Finklea H, Snider DA, Fedyk J, Sabatani E, Gafni Y, Rubinstein I (1993) Langmuir 9:3660–3667
42. Nicholson RS (1965) Anal Chem 37:1351–1355
43. Szroeder P (2011) Phys E 44:470–475
44. Royea WJ, Hamann TW, Brunschwig BS, Lewis NS (2006) J Phys Chem B 110:19433–19442
45. Cline KK, McDermott MT, McCreery RL (1994) J Phys Chem 98: 5314–5319
46. Bowling RJ, Packard RT, McCreery RL (1989) J Am Chem Soc 111: 1217–1223
47. Radchenko TM, Tatarenko VA, Sagalianov YI, Prilutskyy YI (2014) Configurations of structural defects in graphene and their effects on its transport properties. In: Edwards BT (ed) Graphene. Mechanical properties potential applications and electrochemical performance, 1st edn. Nova Publishers, New York, pp 219–259
48. Ross Macdonald J (1987) J Electroanal Chem 223:25–50
49. Qi Y, Rhim SH, Sun GF, Weinert M, Li L (2010) Phys Rev Lett 105: 085502
50. Gueshi T, Tokuda K, Matsuda H (1978) J Electroanal Chem 89:247–260
51. Tokuda K, Gueshi T, Matsuda H (1979) J Electroanal Chem 102:41–48
52. Barreira SVP, García-Morales V, Pereira CM, Manzanares JA, Silva F (2004) J Phys Chem B 108:17973–17982